Effect of Jet Coordination on Underwater Propulsion with the Multi-Robot SALP System

Zhiyuan Yang, Yipeng Zhang, Matthew Herbert, M. Ani Hsieh, and Cynthia Sung

***Abstract*— Salps, marine invertebrates known for their collective swimming through coordinated jet propulsion, offer a unique model for efficient underwater movement. Inspired by this biological system, we develop the SALP (Salp-inspired Approach to Low-energy Propulsion) robot, a soft underwater robot that swims via jet propulsion similarly to a biological salp. The SALPs can be physically connected into SALP chains and coordinate their jets to achieve various propulsion modes. In our experiments, we compare the swimming performance of the individual SALP with the two-SALP system, focusing on power, acceleration, velocity, and energy efficiency. Results indicate that two SALPs swimming synchronously exhibit a 9.0% increase in steady-state velocity and a 16.6% improvement in transient acceleration compared to a single SALP. Additionally, our analysis of swimming efficiency implies that asynchronous swimming is potentially more energy efficient than the synchronous mode, as reflected by a decrease in the cost of transport (COT).**

I. Introduction

Salps – a type of marine invertebrate – are considered some of the world's most efficient swimmers [1], [2]. These soft, tubular creatures use jet propulsion to transport themselves hundreds of meters per day and can be found in every one of the world's oceans. Salps demonstrate a unique locomotion strategy compared to many other underwater swimmers: they grow in physically-connected colonies of up to 80 units and several meters long that travel as a group [3]. In this form, they form multi-jet systems that can synchronize or desynchronize their jets to change their locomotion behavior [3], [4]. In this paper, we explore multi-jet soft robot locomotion using the SALP (Salp-inspired Approach to Low-energy Propulsion) robot (Fig. 1(a)). Similar to actual salps, individual SALPs can be connected into SALP chains and coordinate their jets to achieve different locomotion modes. We evaluate the effect of this coordination on swimming performance compared to individual units by considering the swimming acceleration, speed, and locomotion efficiency.

A. Underwater Swimming Robots

Underwater robots operate beneath the water's surface, performing tasks like exploration, environmental monitoring, and resource harvesting [6]. Traditional rigid underwater vehicles can be limited in maneuverability and efficiency when dealing with the complex dynamical environments caused by oceanic topographies, irregular terrains, and unpredictable currents. Bio-inspired designs have the potential to address these limitations by mimicking the locomotion and morphology of marine animals, offering enhanced agility, energy efficiency, and adaptability [7].

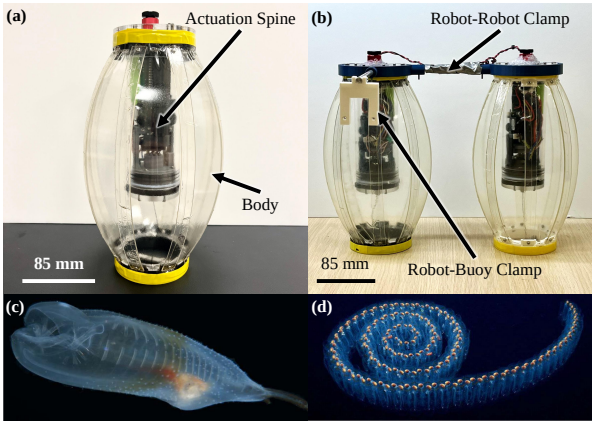

Fig. 1. (a) Single SALP robot design. The robot consists of a soft body and an actuation spine. (b) Two SALPs can be physically connected to coordinate their jets and change locomotion modes. (c) Biological salp serving as inspiration for this project. (d) Biological salp chain. Images in (c,d) are modified from [5], ©2017 IEEE.

Many examples of bio-inspired underwater soft robots [8] have been developed to imitate natural swimming motions, including manta ray-inspired fin undulation [9], eel-like oscillation [10], amphibious turtle-inspired drag-induced swimming [11], starfish-like crawling [12], and squid-like jet propulsion [13], [14]. Among the types of swimming locomotion [8], jet propulsion is a common swimming mode used by biological cephalopods and tunicates (such as squids, cuttlefish, and salps) and commonly imitated in robotics since it is an efficient mode of underwater locomotion [2], [15]. Jet-propelled animals move forward by rapidly changing the volumes of their body, drawing water into their muscular mantle cavity through the openings on the ends of the body, and then expelling it under high pressure through a funnel. This type of locomotion can produce a wide range of forward velocities by varying the contraction of the mantle to generate the propulsive jet [16]. In addition, a pulsed jet generates a larger average thrust than a steady jet of the same mass flow rate [1]. Jet-propelled robotic swimmers similarly capitalize on rapid volumetric changes to enable efficient aquatic locomotion. These designs typically

Support for this project has been provided in part by ONR Award #N00014-23-1-2068 and by NSF Grant No. 2121887.

The authors ZY, YZ, MAH, and CS are with the General Robotics, Automation, Sensing & Perception (GRASP) Laboratory at the University of Pennsylvania, Philadelphia, PA 19104, USA. MH is with Newark Academy, Livingston, NJ 07039. Emails: {annieyzy, yipenggg, mya, crsung}@seas.upenn.edu, matthewherbert25@gmail.com.

include elastomeric [17], [18] or thin plastic [13] shells that allow repeated volumetric change to generate thrust and speed. Actuation methods for creating this volumetric change include tendon-driven control [13], rack-and-pinion [14] or solenoid-piston [15] actuation, as well as smart-material actuators [19], all enabling periodic expansion and contraction for sustained jetting movement.

B. Salps

Among invertebrates using jet propulsion, salps are among the most energy-efficient. Compared to squids, for example, which have a cost of transport (COT) of 0.5-0.7 [20], salps have a much lower COT of 0.11 [21], while still being able to move forward at speeds of 1.0-6.6 cm/s (or approximately 1 body length/s) [22].

Salps can swim both as a solitary jetter (Fig. 1(c)) and connected as a multi-jet colony (Fig. 1(d)). Their aggregate colony forms can contain up to tens of hundreds of identical individuals forming what is known as a "salp chain" [23]. The individuals inside the chain are physically attached through plaques and communicate through transmitting electrical impulses to coordinate swimming [24], [3]. Interestingly, this coordinated swimming can involve either asynchronous or synchronous jetting. In general, synchronous jetting produces higher speeds and accelerations, while asynchronous jetting is more energy-efficient [25], [26]. When it comes to the COT, asynchronous jetting provides hydrodynamic advantages since the steady swimming velocities produced by multiple asynchronous jets lowers drag compared to the periodic acceleration and deceleration produced by synchronous jets [3]. Further, by changing jet timing, wake interactions among swimmers can be leveraged to lower the COT similarly to effects previously found in schools of fish [27]. When more units are connected, the speed and efficiency of salp chains increase, resulting in up to 44% gains in efficiency compared to a solitary salp [22].

C. Multi-robot Underwater Systems

Despite the apparent locomotive benefits of multi-jetting systems, few examples of multi-jet or multi-robot jet-propelled swimmers exist. Underwater robotic swarms generally focus on robotic fish [28], [29], and physically connected swimming robots remain relatively underexplored. At the same time, physically connecting these robots may offer distinct advantages, particularly in challenging underwater environments where maintaining group cohesion is critical. Such systems are less likely to lose individual robots, as the physical connection ensures group integrity even in turbulent waters or strong currents, reducing the risk of communication loss or separation. This physical linkage can enhance stability, coordination, and overall mission reliability. The Roboat [30], [31] and Modboats [32], [33] systems are both low degree-of-freedom systems that connect together to swim more stably as a group, but they are surface vehicle systems and only consider assembly of geometric structures rather than locomotion benefits. We therefore aim to explore this gap in understanding coordinated multi-robot jet propulsion for underwater locomotion.

D. Our Contributions

We investigate multi-jet coordination in the context of a two-SALP physically connected robot system. Our main contributions include:

- the design and experimental evaluation of the SALP robot, an underwater soft untethered jetter, capable of swimming at a speed of 9.46 cm/s (0.34 body lengths/s) with a COT of 2.01;
- the demonstration of the two-SALP system consisting of physically connected SALPs that can contract, release, and coordinate to move;
- the study of swimming performance and efficiency of the two-SALP system with different coordinated swimming modes; and
- the comparison of the single SALP to a two-SALP system in terms of the speed and energy efficiency.

The rest of the paper is structured as follows: Section II presents an overview of the robot design, fabrication, actuation, and control, and how these systems change when multiple SALP robots are connected and must coordinate. Section III describes experimental results on the single SALP and the two-SALP system. Section IV concludes with implications for future work.

II. ROBOT DESIGN

The SALP (Salp-inspired Approach to Low-energy Propulsion, Fig. 1(a)) robot is a soft jet-propelled swimmer similar in design to our previous work [13] and the cephalopod-inspired robot by Christianson et al. [14]. The robot consists of two main elements: a body and an actuation spine. The robot's body (Fig. 2(a)) is designed so that a contraction in length results in an increase in body volume. A nozzle in the rear end cap allows water to enter and exit the robot body. The robot swims by alternately contracting its body to inhale water from its surroundings and rapidly releasing back to the resting state to expel that water as a jet that propels it forward. The actuation spine houses the actuators, sensors, and electronics that power and control this locomotion sequence. The assembled robot is 280 mm in length (including the end caps and power switch), 150 mm in diameter in its resting state, and weighs 585 g.

A. Robot Fabrication

The robot body (Fig. 2 (a)) consists of a skeleton, a skin, and two end caps. The skeleton is constructed using eight compliant beams, each 240 mm in length and 15 mm in width, and laser-cut from 1.27 mm (0.05") thick PETG. The beams are attached by screws to two end caps (Fig. 2 (b)) through rotatable hinges that enable the flexible beams to bend freely within a limited range. The result is a stable structure that tends toward the cylindrical state with the beams straight but that has the ability to compress by bending the beams. In order to prevent the beams from bending inward during compression, a 1.59 mm (1/16") thick acrylic

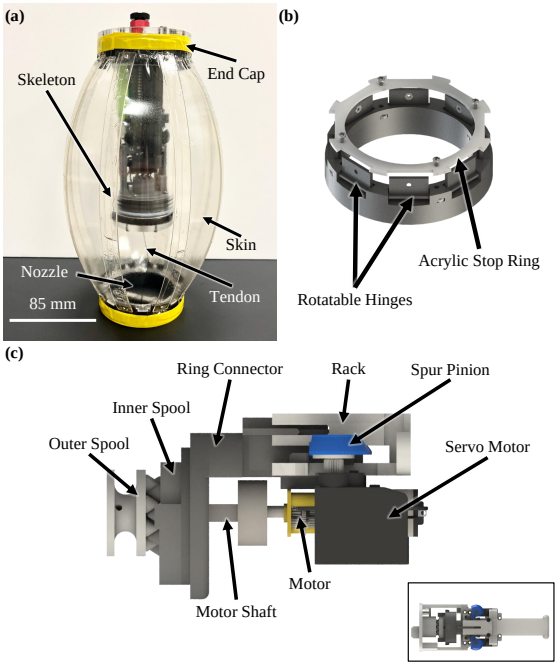

Fig. 2. SALP design breakdown. (a) Overview of the single SALP robot body. The body consists of a skeleton, a skin, and two end caps. A tendon between the actuation spine and the back end cap controls the robot's contraction. (b) End cap design with the rotatable hinges that attach to the compliant beams. An acrylic stop ring limits the range of rotations for these hinges. (c) Actuation mechanism consisting of a spool for pulling the tendon and a rack-and-pinion for engaging and disengaging the spool. The inset on the bottom right shows the top view of the fully assembled mechanism in its housing.

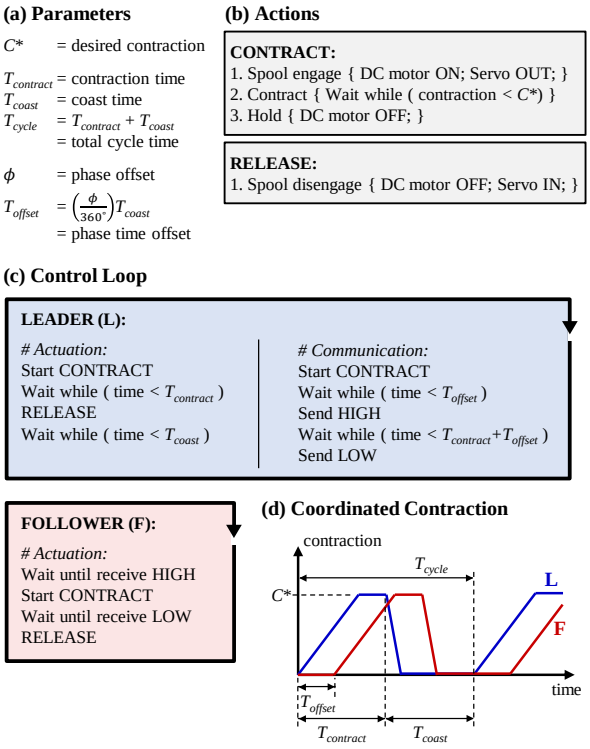

Fig. 3. SALP robot control overview. (a) Control parameters for changing the robot's jetting cycles. (b) Actions of the single SALP robot during contract and release. (c) Control loop and communications within the two-SALP system. (d) Plots of contraction over time for the coordinated two-SALP system with a phase offset.

stop ring is added on top of the hinges, restricting their angle range from 27.6° to 90°. The resulting resting state of the robot is an ellipsoidal shape with the beams bent outward slightly, and the robot consistently expands in volume when contracted in length. To seal the robot so that water can be inhaled and expelled only from the nozzle, the skeleton is covered with a smooth, 0.25 mm (0.010") elastomeric skin made of 3M VHB Adhesive Transfer Tape F9473PC similar to [14]. The resulting body is able to change from a volume of 2947 cm^3 in its resting state to 4020 cm^3 when contracted by 2 cm.

The robot is actuated through a tendon and spool mechanism similar to our previous design [13]. A tendon is attached to the rear end cap and wound around a spool to control the length of the robot. The actuation mechanism (Fig. 2(c)) consists of two main components: a DC motor (Pololu 1000:1 Micro Metal Gearmotor HP 6 V) that rotates the spool and two servomotors (P0025 2.5 g Micro Servo) that drive a rack-and-pinion mechanism to engage and disengage the spool from the DC motor. The rotation of the spool is monitored through a magnetic encoder (Pololu Magnetic Encoder 12 CPR, 2.7-18 V). The system is controlled via an Adafruit Feather M0 Adalogger microcontroller, which monitors the encoder readings and controls the activation of the DC motor and servomotors. In addition, a DC current sensor (Adafruit INA219) collects the electrical power input of all the electronics when the robot is on. To enable untethered swimming, the robot is powered by a 7.4 V 500 mAh lithium-ion battery, with all data saved to the microSD card on the microcontroller. To waterproof the electronics and the actuation system, the circuit and actuation system are all enclosed in a 15.0 cm (5.9") long and 5.08 cm (2") inner diameter acrylic waterproof tube (BlueRobotics), which is screwed to the front cap of the robot body.

B. Locomotion

The SALP robot locomotes by alternating between two actions (Fig. 3(b)): contract and release. In the contraction phase of the actuation cycle, the servomotors move the rack out to engage the spool and the DC motor turns on to pull in the tendon at its maximum speed. Once the robot reaches the desired contraction (C^*) as measured by the encoder, then it turns off the DC motor and holds until the predesignated contraction time ($T_{contract}$). Both contraction amount and contraction time are used to standardize the robot's jet timing because the robot's contraction efficiency may vary depending on the battery's voltage level. The maximum time the robot needs to contract to C^* is defined as $T_{contract}$ and is chosen based on preliminary experiments. In the release phase, the servomotors move the rack in to suddenly disengage the spool, allowing the spool to rotate freely and the robot to rapidly return to its resting state. The robot coasts for T_{coast} before repeating the cycle.

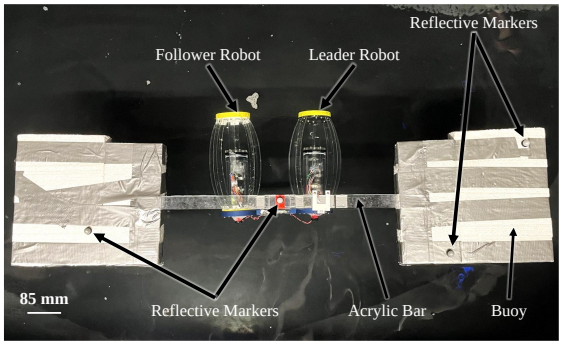

Fig. 4. Experimental setup for two-SALP swimming tests.

C. Two-SALP Connection and Coordination

To investigate the effect of coordinated swimming compared to individual units, two SALPs are physically attached through the rigid connection shown in Fig. 1(b). This rigid connection consists of two circular 3D-printed clamps that attach to the front caps of the robots and an aluminum rod between them. The connections are designed to make two robots swim inline and in parallel at a fixed offset distance. The length of the middle rod (10 cm) is calculated based on the change in body radius experienced by the robots under 2 cm contraction and is the minimum necessary to prevent the robots from colliding with each other.

For coordinated swimming, a signal wire is attached between the microcontrollers of the two SALPs. We define one as the Leader SALP (L) and the other as the Follower SALP (F). The Leader SALP controls its own jetting based on the given control parameters and sends high and low signals to the Follower to trigger its contract and release actions (Fig. 3(c)) according to the desired phase offset (ϕ) so that the two robots' clocks can be synchronized. In particular, the robot computes the total jet cycle time as $T_{cycle} = T_{contract} + T_{coast}$ and the phase time offset between the two robots as $T_{offset} = \frac{\phi}{360^\circ} T_{cycle}$. Whenever the Leader initiates a contract action, it waits T_{offset}, then sends a high signal to the follower to trigger the Follower's contraction. Similarly, whenever the leader initiates a release, it waits T_{offset}, then sends a low signal to the Follower to trigger the Follower's release. A phase offset of $\phi = 0^\circ$ indicates that the SALPs are synchronizing their jets. Fig. 3(d) shows the resulting contraction and release cycles of the coordination.

III. UNDERWATER EXPERIMENTS

We evaluate the robot's performance by conducting a swimming test in a 4.5 m $\times$ 3 m water tank with 18" water depth. In its natural state, the robot floats half-submerged. To fully submerge the robot underwater, we design a rigid robot-buoy clamp with a length of 15 cm and connect it to the front end cap. As shown in Fig. 4, the clamp is attached to a rigid floating buoy that keeps the robot entirely underwater. Four reflective markers are affixed to the floating buoy for tracking with an OptiTrack motion capture system consisting of thirteen Prime 13 cameras. One marker is registered at the center of the robot system. Real-time power and encoder data

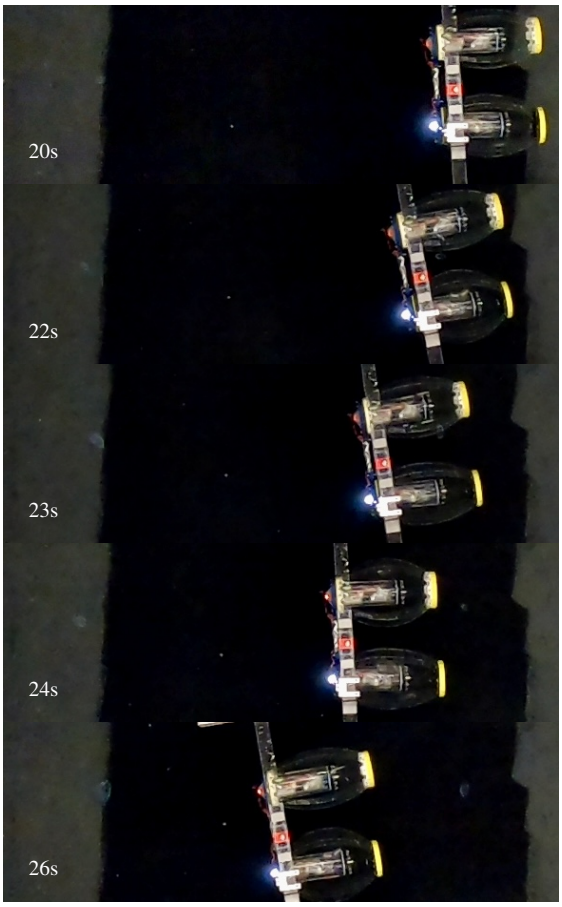

Fig. 5. Snapshots of the two-SALP system with phase offset $\phi = 180^\circ$, from the beginning of the sixth actuation cycle.

are saved to the microSD card on the robot and retrieved at the end of each trial. The robot's motion is also recorded using an overhead high-resolution camera (GoPro Hero 8 Black) mounted 2.0 m above the center of the tank.

A. Single Robot Performance Analysis

We start by characterizing the single SALP robot for comparison with the two-SALP system. We command the robot to execute actuation cycles with $C^* = 2$ cm, $T_{contract} = 2$ s, and vary the coast time as $T_{coast} = \{1, 2, 3\}$ s. Due to the size of the tank, we chose the contraction amount of 2 cm instead of 6 cm (full contraction) to be able to achieve steady-state swimming. The robot is able to consistently achieve the desired contraction and swim forward in the tank. In the underwater experiments, we observe that during the first actuation cycle, the robot remains mostly stationary with slight rotations caused by deformation. Starting from the second actuation cycle, we observe the robot moving forward, and over the next few actuation cycles, its speed increases. The speed stabilizes by the time it reaches the opposite side of the tank.

Fig. 6 shows the results for one trial with $T_{coast} = 2$ s. The velocity curve shows periodic acceleration and deceleration of the robot, with deceleration occurring during contraction

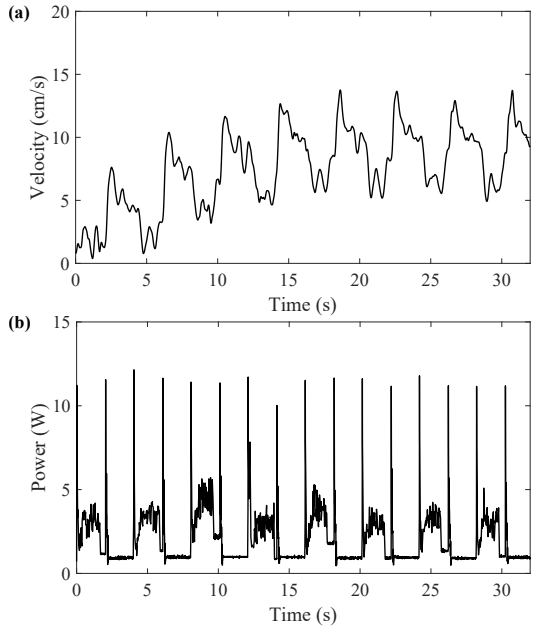

Fig. 6. Plots of (a) velocity over time and (b) power over time for a single SALP performance test with $T_{coast} = 2$ s.

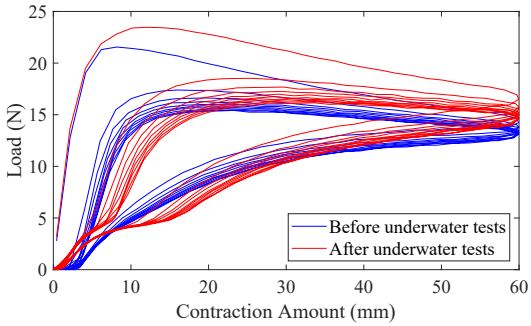

Fig. 7. Force-displacement profile of the single SALP robot before and after underwater tests. The plots show little change in skin behavior over the length of the experiments.

and acceleration during release, and are consistent with previous single-aperture jet-propelled systems [13], [14]. It takes 13 actuation cycles for the robot with $C^* = 2$ cm and $T_{coast} = 1$ s, 11 actuation cycles with $C^* = 2$ cm and $T_{coast} = 2$ s, and 9-10 actuation cycles with $C^* = 2$ cm and $T_{coast} = 3$ s to swim across the long edge of the tank.

Overall, the robot tends to reach a steady average velocity by the end of the fifth actuation cycle. Thus, we split the data into two sections: transient (cycles 1-5) and steady state (cycles 5+). Table I shows the resulting average power consumption, acceleration, velocity, and cost of transport for the robot in each of these two sections. The electrical power consumption is measured by the current sensor on the robot and logged at a frequency of 80 Hz. The average power consumption of the robot is then found by integrating the area under the power curve and dividing the result by the duration of the respective time. The velocity is computed by filtering position data from the motion capture system using a low-pass filter with 1 Hz cutoff frequency and filter order of 20, and then computing finite differences. Then the average transient acceleration is computed by dividing the average velocity of the fifth actuation cycle by 5 (the number of actuation cycles). Finally, the cost of transport is calculated using $COT = P/(mgv)$, where P is the electrical power consumption, $m = 1.13$ kg is the total mass of the system including the mass of the robot, the clamps, and the buoy, v is the average velocity, and g is the gravitational acceleration.

The robot is able to move forward in the water with a maximum steady state velocity of 9.46 cm/s, which translates to 0.34 body lengths/s. Although there is no obvious difference in average transient velocity between the different coast times, the steady-state velocity increases with shorter coast time with $T_{coast} = 1$ s having the highest velocity. However, the power consumption during both transient and steady-state has a decreasing trend with longer coast time. As shown in Fig. 6, each actuation cycle is characterized by two phases: a high-power phase and a low-power phase. An initial peak in power consumption corresponds to the starting up of the motors at the beginning of the jetting cycle, while the high-power phase aligns with the robot's contraction phase. The second peak is associated with the activation of the two servomotors. The low-power phase corresponds to the release and coasting period and is the circuit's minimal power consumption when the robot is inactive. During this phase, the power readings remain relatively stable. The average power during the coasting phase (0.92 W) is much lower than the contraction phase (2.35 W) since there is no actuator running. Combining these trends, the robot with a longer coasting time is able to achieve a much lower transient COT, although by the time the robot reaches steady state, the COT is similar across all conditions (2.01 for $T_{coast} = 1$ s and 2.12 for $T_{coast} = 3$ s).

a) Robot Variations: To establish a fair baseline, we conduct single-robot tests on a second SALP robot (which acts as the follower in the two-robot tests), using $C^* = 2$ cm and $T_{coast} = 2$ s. The results are included in Table I, showing that the performance between the two robots is fairly similar, indicating that the design and fabrication of the design are repeatable and scalable to multi-robot systems. The last row in Table I shows the mean and standard deviation over all the test trials on both SALPs under the same conditions.

b) Skin Characterization: All reported experiments are conducted on the same robot and skin. Since soft robots of this type may experience fatigue with repeated deformation, which will impact the swimming performance of the robot, we also characterize the force response of the skin before and after experiments. We experimentally measure the force-displacement profile of the robot body on an MTS Criterion C41 machine with a 1 kN load cell. Given the restricted length of the water-sealed spine for electronics, the maximum contraction amount of the robot is 60 mm. The robot is compressed 60 mm and released to its original state by the MTS machine for 10 continuous cycles at a speed of 20 mm/s. As shown in Fig. 7, the force in the first cycle reaches a maximum of 22 N at around 10 mm of contraction

TABLE I. Single SALP performance with varying coast time T_{coast}

Parameters			Transient				Steady State		
Robot ID	C^* (cm)	T_{coast} (s)	Power (W)	Acceleration (cm/s/cycle)	Velocity (cm/s)	Cost of Transport	Power (W)	Velocity (cm/s)	Cost of Transport
L	2	1	2.64 (0.24)	1.68 (0.10)	5.56 (0.28)	4.30 (0.16)	2.10 (0.14)	9.46 (0.37)	2.01 (0.18)
L	2	2	2.16 (0.10)	1.58 (0.15)	5.71 (0.65)	3.46 (0.39)	1.92 (0.07)	8.53 (0.25)	2.03 (0.10)
L	2	3	1.93 (0.12)	1.54 (0.11)	5.85 (0.32)	3.00 (0.33)	1.80 (0.12)	7.66 (0.08)	2.12 (0.14)
F	2	2	2.33 (0.21)	1.57 (0.09)	6.02 (0.50)	3.54 (0.54)	1.95 (0.08)	8.02 (0.27)	2.20 (0.08)
L & F	2	2	2.26 (0.19)	1.57 (0.12)	5.89 (0.59)	3.50 (0.48)	1.94 (0.08)	8.24 (0.36)	2.13 (0.12)

Values are reported in the notation "mean (standard deviation)". All tests are conducted with $C^* = 2$ cm.
L & F represents the combination of all test trails on L and F.

TABLE II. Two-SALP performance with varying phase offset ϕ

Parameters	Transient				Steady State		
ϕ (°)	Power (W)	Acceleration (cm/s/cycle)	Velocity (cm/s)	Cost of Transport	Power (W)	Velocity (cm/s)	Cost of Transport
0	4.03 (0.28)	1.83 (0.19)	6.99 (0.69)	3.35 (0.12)	3.55 (0.13)	8.98 (0.63)	2.30 (0.18)
90	4.01 (0.25)	1.82 (0.13)	6.45 (0.46)	3.62 (0.30)	3.47 (0.07)	9.08 (0.93)	2.24 (0.23)
180	3.33 (0.12)	1.74 (0.21)	5.95 (0.67)	3.28 (0.26)	3.25 (0.09)	8.75 (0.69)	2.16 (0.11)

Values are reported in the notation "mean (standard deviation)". All tests are conducted with $C^* = 2$ cm and $T_{coast} = 2$ s.

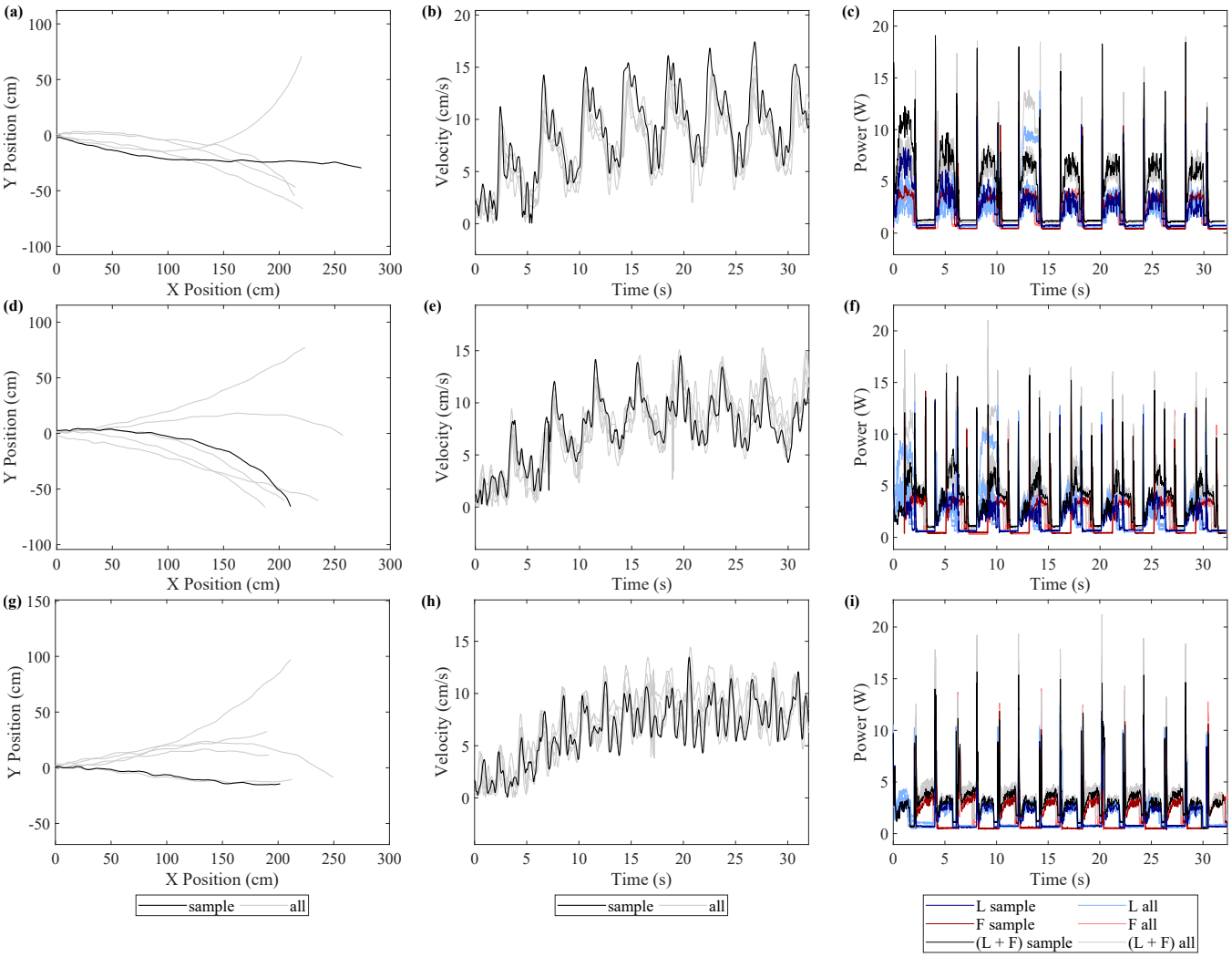

Fig. 8. Results for two-SALP experiments. Rows are arranged as (top) $\phi = 0°$, (middle) $\phi = 90°$, and (bottom) $\phi = 180°$. Plots show (a,d,g) X-Y trajectories of the robots, (b,e,h) velocity over time, and (c,f,i) power over time. For all plots, results from all experimental trials are shown in light colors, with a sample trial for each condition highlighted in a darker color for better visualization.

and decreases to 14 N at 60 mm of contraction. Over the 10 cycles, the force curve flattens to remain constant at around 15 N after 10 mm of contraction. The curves before and after the underwater tests look approximately the same. There is a slight increase in the force experienced by the skin in the first compression cycle, likely due to changes in skin viscosity caused by water flow, but since the swimming tests all involve trials with at least 10 jetting cycles, we conclude that skin fatigue should have no great impact on the conclusions of the swimming tests.

B. Two-robot Performance with Synchronous and Asynchronous Swimming

Motivated by biological studies of salps, we test the two-SALP system swimming in parallel and compare the performance and efficiency with a single robot. We keep the actuation parameters as $C^* = 2$ cm and $T_{coast} = 2$ s, which is the center of the single robot test grid.

To explore the effect of coordination, we set the phase offset between the jet propulsion of the two robots as $\phi = \{0°, 90°, 180°\}$. Similar to the single-SALP experiments, all the trials of the two-SALP system can move forward and reach steady-state velocity by the end of the fifth actuation cycle. We observed that the two-SALP system with asynchronous swimming experiences more oscillations (Fig. 5), which makes sense since the robots being offset from the center of the system will generate a torque on the system during jetting. This effect also has an impact on the overall velocity of the system. Fig. 8(b,e,h) shows plots of the velocity of the system with different phase offsets. We find that the $\phi = 0°$ has only one propulsion peak per actuation cycle, which is the same as the single-SALP's behavior. However, the sizes of these peaks decrease and more oscillations in velocity become apparent for $\phi = 90°$ and $\phi = 180°$.

Summary statistics from the two-robot experiments are shown in Table II. The data is processed in the same way as for the single-robot tests, except that a mass of $m = 1.76$ kg is used for the COT calculation to account for the two robots, the clamps, and the buoy. The results show that power consumption during both transient and steady-state swimming decreases from $\phi = 0°$ to $\phi = 180°$ as the robots desynchronize. However, the velocity of the system also decreases as the robots desynchronize. Combining these together, we find a decreasing trend in steady state cost of transport as the robots change from phase offset $\phi = 0°$ to $\phi = 180°$. These results are consistent with biological hypotheses that asynchronous swimming is potentially more efficient while synchronous swimming provides higher velocities [26], [25].

a) Comparison to single SALP: Comparing the two-SALP system to the single SALP, we find that the two-SALP system experiences larger transient accelerations and larger velocities. The two-SALP system with $\phi = 0°$ has a transient acceleration of 1.83 cm/s/cycle which is 16.6% higher than the average of the two single-SALP robots at 1.57 cm/s/cycle. In addition, the two-SALP system with $\phi = 0°$ has an average steady-state velocity of 8.98 cm/s, which is 9.0% higher than the average steady-state velocity (8.24 cm/s) of the two single-SALP robots. This finding matches the biological hypotheses [25] that speeds increase with more swimming units.

Considering the energetic efficiency, we find that the COT for the two-SALP system is higher than that of the single SALP. Studies of biological multijet systems have shown substantial COT savings, which is contrary to our results. However, the energetic benefit seems to increase as the number of units in the system becomes larger [26], and it is possible that the benefits are not pronounced for 2-unit systems. Further, more units will provide extra redundancy in the system for steering, robustness against unit failure or battery drainage, and more options to further even out the velocity profile of the system. Thus, additional experiments with more SALPs are required to evaluate the tradeoffs of single-jet and multi-jet versions.

IV. CONCLUSIONS

In this paper, we describe the SALP robot system and demonstrate its locomotion capabilities in both solitary and two-robot swimming with physically-connected robots. We find that a single SALP robot has a maximum steady state velocity of 9.46 cm/s (0.34 body lengths/s). The velocity increases by 9.0% when two robots are connected together. Further, the two-SALP system is able to achieve a 16.6% higher transient acceleration. These findings suggest that the two-SALP system has advantages in swimming performance. We also find that coordinated jetting can change the cost of transport of the robot system, with in-phase jetting producing higher COT and out-of-phase jetting producing lower COT. This indicates that asynchronous swimming is potentially more energy-efficient than synchronous swimming.

More investigations must be performed to better understand the strengths and limitations of a physically connected multi-jet robot system. In particular, in biological salp chain structures, some physical offset among the salps helps limit the overall cross-sectional area of the system, reducing the drag [3]. By reducing the interaction between the chain and the surrounding fluid, the system can become more hydrodynamically efficient. As a result, this characteristic plays a significant role in improving the chain's performance in aquatic environments. In this paper, we place the robots side-by-side in the most drag-inefficient configuration. In the next steps, we plan to vary the physical offset between the two robots to investigate these drag changes and their relationship with the robot's COT. Further, since the COT of multi-jetting organisms in nature is related not only to the swimming mode but also to the colony length [26], we will conduct further experiments with more robots to see if the COT drops when more robots are added to the chain.

Future work also includes investigating the potential for multi-jetting systems to improve the maneuverability of the robot. During experiments, we find that out-of-phase behavior in the two-robot system produces asymmetric jetting that torques the system. This torque may produce a natural

method of steering for the system, where units placed at different spatial locations may coordinate their jet timing to turn the system or keep it moving straight.

Finally, swimming is a multifaceted activity influenced by various factors beyond just the robot's mass, shape, and electronics. Additional hydrodynamic forces and fluid-structure interactions affect the robot's performance in water. Thus, understanding the behavior of the surrounding fluid will play a critical role in determining and optimizing the overall effectiveness and efficiency of the robot's movement. We intend to conduct experiments to better understand the effects of the fluid-structure interactions on robot's jetting behavior, and the effect of multiple robots' jets on each other. Looking forward, the SALP platform will enable further exploration into how the flow field enhances the performance and efficiency of a salp-inspired multi-robot system.

ACKNOWLEDGEMENT

The authors would like to thank Dr. Kelly Sutherland for inspiring discussions about salps; Victoria Edwards for OptiTrack system setup; Jeremy Wang, Britny Major, Ari Bortman, and Peter Bruno for fabrication advice and assistance; and Tate Park, Siddharth Panchanadam, Bruke Baraki, and Xueyang Qi for help with robot design and assembly.

REFERENCES

[1] B. J. Gemmell, J. O. Dabiri, S. P. Colin, J. H. Costello, J. P. Townsend, and K. R. Sutherland, "Cool your jets: Biological jet propulsion in marine invertebrates," *Journal of Experimental Biology*, vol. 224, no. 12, p. jeb222083, 2021.

[2] B. J. Gemmell, J. H. Costello, S. P. Colin, C. J. Stewart, J. O. Dabiri, D. Tafti, and S. Priya, "Passive energy recapture in jellyfish contributes to propulsive advantage over other metazoans," *Proceedings of the National Academy of Sciences*, vol. 110, no. 44, pp. 17 904–17 909, 2013.

[3] K. R. Sutherland and D. Weihs, "Hydrodynamic advantages of swimming by salp chains," *Journal of The Royal Society Interface*, vol. 14, no. 133, p. 20170298, 2017.

[4] G. Mackie and Q. Bone, "Locomotion and propagated skin impulses in salps (Tunicata: Thaliacea)," *The Biological Bulletin*, vol. 153, no. 1, pp. 180–197, 1977.

[5] S. Guo, S. Sun, and J. Guo, "Design of a SMA-based salps-inspired underwater microrobot for a mother-son robotic system," in *IEEE International Conference on Mechatronics and Automation (ICMA)*, 2017, pp. 1314–1319.

[6] R. Bogue, "Underwater robots: A review of technologies and applications," *Industrial Robot: An International Journal*, vol. 42, no. 3, pp. 186–191, 2015.

[7] Z. Cui, L. Li, Y. Wang, Z. Zhong, and J. Li, "Review of research and control technology of underwater bionic robots," *Intelligent Marine Technology and Systems*, vol. 1, no. 1, p. 7, 2023.

[8] S. M. Youssef, M. Soliman, M. A. Saleh, M. A. Mousa, M. Elsamanty, and A. G. Radwan, "Underwater soft robotics: A review of bioinspiration in design, actuation, modeling, and control," *Micromachines*, vol. 13, no. 1, p. 110, 2022.

[9] T. Yang and Z. Chen, "Development of 2D maneuverable robotic fish propelled by multiple ionic polymer-metal composite artificial fins," in *IEEE International Conference on Robotics and Biomimetics (ROBIO)*, 2015, pp. 255–260.

[10] C. Christianson, N. N. Goldberg, D. D. Deheyn, S. Cai, and M. T. Tolley, "Translucent soft robots driven by frameless fluid electrode dielectric elastomer actuators," *Science Robotics*, vol. 3, no. 17, p. eaat1893, 2018.

[11] R. L. Baines, J. W. Booth, F. E. Fish, and R. Kramer-Bottiglio, "Toward a bio-inspired variable-stiffness morphing limb for amphibious robot locomotion," in *2nd IEEE International Conference on Soft Robotics (RoboSoft)*, 2019, pp. 704–710.

[12] S. Mao, E. Dong, H. Jin, M. Xu, S. Zhang, J. Yang, and K. H. Low, "Gait study and pattern generation of a starfish-like soft robot with flexible rays actuated by smas," *Journal of Bionic Engineering*, vol. 11, no. 3, pp. 400–411, 2014.

[13] Z. Yang, D. Chen, D. J. Levine, and C. Sung, "Origami-inspired robot that swims via jet propulsion," *IEEE Robotics and Automation Letters*, vol. 6, no. 4, pp. 7145–7152, 2021.

[14] C. Christianson, Y. Cui, M. Ishida, X. Bi, Q. Zhu, G. Pawlak, and M. T. Tolley, "Cephalopod-inspired robot capable of cyclic jet propulsion through shape change," *Bioinspiration & Biomimetics*, vol. 16, no. 1, p. 016014, 2020.

[15] T. Bujard, F. Giorgio-Serchi, and G. D. Weymouth, "A resonant squid-inspired robot unlocks biological propulsive efficiency," *Science Robotics*, vol. 6, no. 50, p. eabd2971, 2021.

[16] I. K. Bartol, P. S. Krueger, W. J. Stewart, and J. T. Thompson, "Hydrodynamics of pulsed jetting in juvenile and adult brief squid Lolliguncula brevis: Evidence of multiple jet 'modes' and their implications for propulsive efficiency," *Journal of Experimental Biology*, vol. 212, no. 12, pp. 1889–1903, 2009.

[17] F. G. Serchi, A. Arienti, I. Baldoli, and C. Laschi, "An elastic pulsed-jet thruster for soft unmanned underwater vehicles," in *IEEE International Conference on Robotics and Automation (ICRA)*, 2013, pp. 5103–5110.

[18] F. Giorgio-Serchi, F. Renda, M. Calisti, and C. Laschi, "Thrust depletion at high pulsation frequencies in underactuated, soft-bodied, pulsed-jet vehicles," in *IEEE OCEANS*, 2015, pp. 1–6.

[19] A. Jones and J. R. Davidson, "Underwater salp-inspired soft structure contraction with twisted coiled actuators," in *IEEE 7th International Conference on Soft Robotics (RoboSoft)*, 2024, pp. 504–510.

[20] R. O'dor, J. Wells, and M. Wells, "Speed, jet pressure and oxygen consumption relationships in free-swimming Nautilus," *Journal of Experimental Biology*, vol. 154, no. 1, pp. 383–396, 1990.

[21] E. Trueman, Q. Bone, and J. Braconnot, "Oxygen consumption in swimming salps (Tunicata: Thaliacea)," *Journal of Experimental Biology*, vol. 110, no. 1, pp. 323–327, 1984.

[22] Q. Bone and E. Trueman, "Jet propulsion in salps (Tunicata: Thaliacea)," *Journal of Zoology*, vol. 201, no. 4, pp. 481–506, 1983.

[23] K. R. Sutherland and L. P. Madin, "Comparative jet wake structure and swimming performance of salps," *Journal of Experimental Biology*, vol. 213, no. 17, pp. 2967–2975, 2010.

[24] P. Anderson and Q. Bone, "Communication between individuals in salp chains. II. Physiology," *Proceedings of the Royal Society of London. Series B. Biological Sciences*, vol. 210, no. 1181, pp. 559–574, 1980.

[25] K. R. Sutherland, A. Damian-Serrano, K. T. Du Clos, B. J. Gemmell, S. P. Colin, and J. H. Costello, "Spinning and corkscrewing of oceanic macroplankton revealed through in situ imaging," *Science Advances*, vol. 10, no. 20, p. eadm9511, 2024.

[26] K. T. Du Clos, B. J. Gemmell, S. P. Colin, J. H. Costello, J. O. Dabiri, and K. R. Sutherland, "Distributed propulsion enables fast and efficient swimming modes in physonect siphonophores," *Proceedings of the National Academy of Sciences*, vol. 119, no. 49, p. e2202494119, 2022.

[27] K. Doi, T. Takagi, Y. Mitsunaga, and S. Torisawa, "Hydrodynamical effect of parallelly swimming fish using computational fluid dynamics method," *PLOS One*, vol. 16, no. 5, p. e0250837, 2021.

[28] J. Salazar, L. Cai, B. Cook, and D. Rus, "Multi-robot visual control of autonomous soft robotic fish," in *IEEE/OES Autonomous Underwater Vehicles Symposium (AUV)*, 2022, pp. 1–6.

[29] F. Berlinger, M. Gauci, and R. Nagpal, "Implicit coordination for 3D underwater collective behaviors in a fish-inspired robot swarm," *Science Robotics*, vol. 6, no. 50, p. eabd8668, 2021.

[30] W. Wang, Z. Wang, L. Mateos, K. W. Huang, M. Schwager, C. Ratti, and D. Rus, "Distributed motion control for multiple connected surface vessels," in *IEEE/RSJ International Conference on Intelligent Robots and Systems (IROS)*, 2020, pp. 11 658–11 665.

[31] S. Park, E. Kayacan, C. Ratti, and D. Rus, "Coordinated control of a reconfigurable multi-vessel platform: Robust control approach," in *IEEE International Conference on Robotics and Automation (ICRA)*, 2019, pp. 4633–4639.

[32] G. Knizhnik and M. Yim, "Design and experiments with a low-cost single-motor modular aquatic robot," in *IEEE 17th International Conference on Ubiquitous Robots (UR)*, 2020, pp. 233–240.

[33] ——, "Amplitude control for parallel lattices of docked modboats," in *IEEE International Conference on Robotics and Automation (ICRA)*, 2022, pp. 3027–3033.